Subproject C4.6

Support Interactions and Thermal Stability of Size Selected Clusters Deposited onto Single-Crystal Surfaces

Principle Investigator: Prof. Dr. Manfred Kappes

CFN-Financed Scientists:

Further Scientists: Prof. Dr. Reinhart Ahlrichs, Dr. Artur Böttcher, Dr. Nedko Drebov, Dr. Oliver Hampe[a], Dr. Detlef Schooss[a], Dr. Patrick Weis

Institut für Physikalische Chemie
Karlsruher Institut für Technologie (KIT), Campus Süd

[a]Institut für Nanotechnologie
Karlsruher Institut für Technologie (KIT), Campus Nord

Introduction and Summary

Top-down nanofabrication in its quest for smaller structures eventually runs into the problem of granularity. Chemistry calls these grains clusters. Arguably, harnessing such clusters and their quantum-size effects (in which typically every atom counts) presently remains the greatest challenge for atomically precise nanotechnology in the sub 5 nanometer size range. Towards this end it is necessary to understand structure and quantum size effects for clusters both in their isolated reference states as well as under realistic, surface-trapped conditions. In the previous project period, we have pursued a two pronged approach to address these issues. On the one hand, we have applied several complementary experimental methods for gas-phase cluster structure determination in order to determine the "reference states" under rigorous control of nuclearity and in the absence of matrix interactions. Primarily ion mobility mass spectrometry (IMS), trapped ion electron diffraction (TIED), collision-induced-dissociation (CID) and probes of radiative association kinetics were used for this purpose (together with density functional calculations (in collaboration with C3.1 and C3.3)). On the other hand, we have deposited mass selected clusters onto clean surfaces by soft-landing and have used surface spectroscopies (X-ray- and UV photoelectron spectroscopy (XPS and UPS), thermal desorption spectroscopy (TDS) and Raman) as well as microscopic imaging methods (scanning-force/-tunnelling microscopies (AFM and STM), and electron microscopy (HRTEM and SEM)) to study cluster structures and their substrate interactions.

Gas-phase clusters: Structure sensitive experiments in combination with high level density functional theory (itself combined with structure search procedures based on genetic algorithms) have allowed structure determination for homonuclear clusters of boron, copper, silver, tin, lead and gold in various charge states and for sizes ranging up to 100 atoms. We find that small boron cluster cations form near-planar structures and evolve at larger sizes (from n=16 on) to tubular geometries. Silver cluster cations and anions have icosahedral-type geometries. Gold clusters manifest a wide diversity of structural types ranging from planar, through hollow three-dimensional at intermediate sizes to low symmetry volume filling at larger sizes. Tin clusters were observed to comprise "clusters-of-clusters" structures containing particularly energetically favorable units such as Sn_7 and Sn_{10}^-, which are quite loosely interlinked. Lead clusters are in some respects similar to tin, however the larger clusters are significantly more compact as a general rule. We have also studied a variety of heteronuclear clusters notably doped gold cluster species. In the case of MAu_{16}^- (M=Fe, Co, Ni) we find clear evidence for gold cages which incorporate the magnetic heteroatom. Interestingly, while experimental data can sometimes only be fit by assuming a superposition of multiple coexisting isomeric forms, most clusters in the size range considered appear to comprise only one structure. Typically, this is either the DFT minimum or an energetically close-lying isomer. This having been said, comparison to experiment has also sometimes uncovered systematic problems with DFT descriptions - as for gold clusters in the region of the 2-D to 3-D topological transition.

Deposited clusters: Low energy deposition of mass selected non-IPR (=non isolated pentagon ring) fullerene cages onto clean graphite surfaces has been used to prepare a range of novel nanocarbon films comprising covalently interlinked monodispersed carbon clusters. These are arguably the first examples of cluster materials in which bonding interactions are weak enough to allow subsequent sublimation of individual (intact) cage units from the deposits at elevated temperatures but strong enough to lead to significant modifications of physical and chemical properties – compared to conventional v.d. Waals bound IPR fullerene solids. We have probed some of these solid state properties (e.g. thermal stability, electronic band structure, vibrational/phonon spectra, fulleride formation via cesium intercalation, hydrogenation/ dehydrogenation reactions) as a function of film thickness and substrate. Deposited cages typically correspond to the lowest energy isomeric form of a given size. In a number of cases, e.g. $C_{60}(I_h)$ and $C_{60}(C_{2v})$ several isomers have been found to coexist in the deposits for appropriate incident ion beam conditions.

1. Gas-phase structural probes of clusters

A prerequisite for understanding and applying refractory element clusters on surfaces is knowledge of geometric and electronic structures of the same species in gas-phase. We have correspondingly studied a number of gas-phase cluster systems, with the specific aim of determining the evolution of cluster structure with number of constituent atoms. Below we provide a summary of our results after a short description of the experimental methods used. These were chosen to complement each other regarding the optimal size range for a given cluster structure determination. Cluster geometries were assigned using a synergetic approach in which measurements were fit using structural models derived from DFT-calculations.

1.1. Experimental methods

Ion mobility spectrometry

In gas phase ion mobility spectrometry (IMS), a mass selected ion packet is injected into a drift cell filled with several mbar of helium gas, wherein it is guided by a weak electric field to an exit aperture (and mass spectrometer detector). Its drift time can be converted into a collision cross section, which is directly connected to the ion's geometric shape. In combination with quantum chemical calculations, which can be used to predict collision cross sections for possible isomeric structures, this method allows for structure determination of gaseous cluster ions. We have performed IMS measurements on clusters of boron, tin and lead. In a number of cases, the apparatus was also run at higher drift cell injection energies to allow for studies of collision-induced-dissociation (CID).

Trapped Ion Electron Diffraction

During the last project period TIED has been used to determine the structures of copper, silver, gold and tin ions as a function of cluster size and charge. The experimental setup used for the measurements is schematically shown in Fig. 1. Cluster ions are generated in a magnetron sputter cluster source, mass selected and trapped in a quadrupole ion trap. All measurements were conducted at a trap temperature of ca. 100 K. High energy electrons (40 keV) are scattered by the cluster ions and detected on a phosphor-screen assembly. The scattering pattern is integrated by an external CCD-camera. Details of the experimental setup and the data reduction procedure are given in given in ref [1] and [C4.6:5].

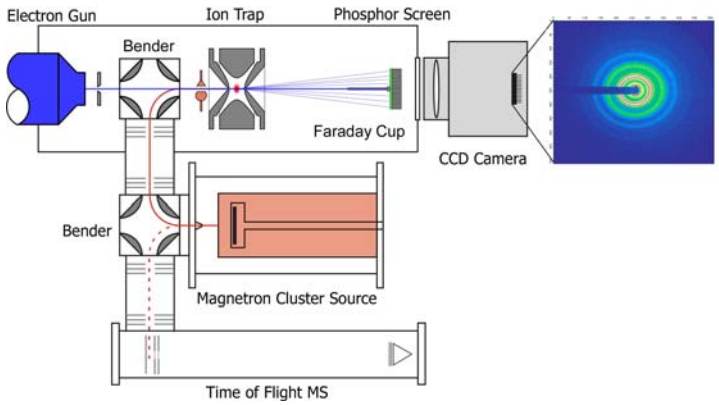

Fig. 1: Experimental setup for TIED. Also shown is a background corrected CCD-image (in false colours) for Ag_{55}^{+}

Ion chemistry probes of metal cluster cations

Low-pressure ion chemistry of metal cluster ions with CO was studied in a Penning trap (= ICR cell) of an FT-ICR mass spectrometer under strictly size-selective conditions. From the measured ion kinetics under few-collision conditions we were able to deduce thermochemical data like the heat of adsorption and its specific cluster size dependence. In order to do so, a detailed modelling of the prevailing reaction mechanism usually termed "radiative association kinetics" was applied. We recently augmented this instrument by a temperature variable ICR cell allowing the study of ions by varying their internal temperature within a range of 100-400K. Again, these experiments were complemented by high level *ab-initio* quantum chemical computations at various levels also using wavefunction based methods as well as density-functional theory (DFT).

1.2. Silver clusters

The first cluster series we have studied by TIED was a range of medium sized silver cluster cations (Ag_n^+ n=19, 38, 55, 59, 75 and 79). We focused our study on sizes where a geometric closed shell structure was to be expected (e.g. Ag_{38} – truncated octahedron, Ag_{55} Mackay icosahedron or Ag_{75} truncated decahedron).

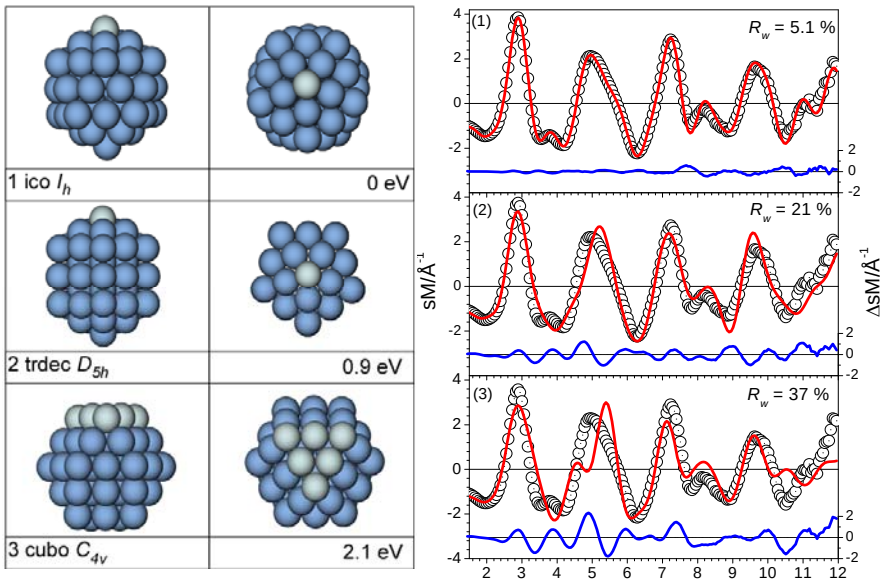

Fig. 2: Left: Minimum energy structures found for various Ag_{55}^+ structural motifs using density function theory calculations. Right: Comparison of experimental (open circles) and model (line) modified molecular scattering functions for the three different isomers of Ag_{55}^+. The lower traces show the residuals. All of the measurements were performed at a trap temperature of 95±1 K. The weighted profile factor R_w is a measure of agreement of experimental and simulated scattering function.

By comparison of experimental and simulated molecular scattering functions obtained from density functional theory (DFT) calculations, we have found that in all cases icosahedral structures were present, suggesting that an icosahedral growth sequence prevails [C4.6:5].

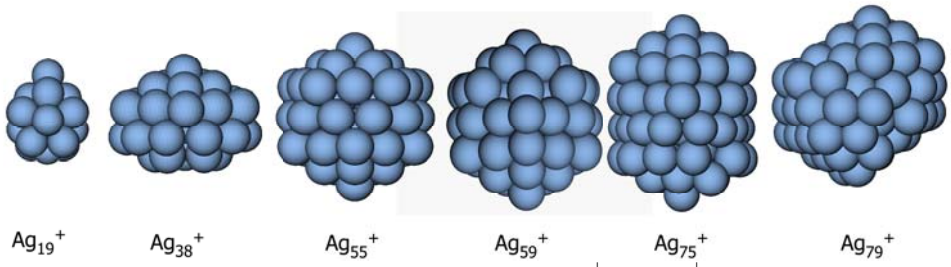

Fig. 3: Structures of Ag_{19}^+ - Ag_{79}^+

1.3. Gold clusters

Gold cluster anions

Small gold cluster anions up to Au_{13}^- have already been studied by IMS [1]. An unexpected result of that work was the identification of planar ground state structures up to quite large cluster sizes. The first 3D structure was found to occur at n=12. However, density functional calculations [2,3,4] predict the transition at even larger sizes. As a possible explanation it was suggested that the experimental observations in this size range were due to a super-cooled metastable 3D phase [4]. To explore whether this is in fact the case, (additional) TIED experiments have been conducted in the 2D-3D transition regime [C4.6:18]. Based on these TIED data (see Fig. 4) Au_{11}^- is a 2D structure. For Au_{12}^- a mixture of two different structural motifs was necessary to fit the experimental data. The major component is a 3D structure, the minor component a flat isomer. Au_{13}^- was found to be a 3D cluster. These results were fully consistent with former IMS measurements using a different cluster source – confirming that standard DFT approaches fail in accurately predicting relative energies in this size range.

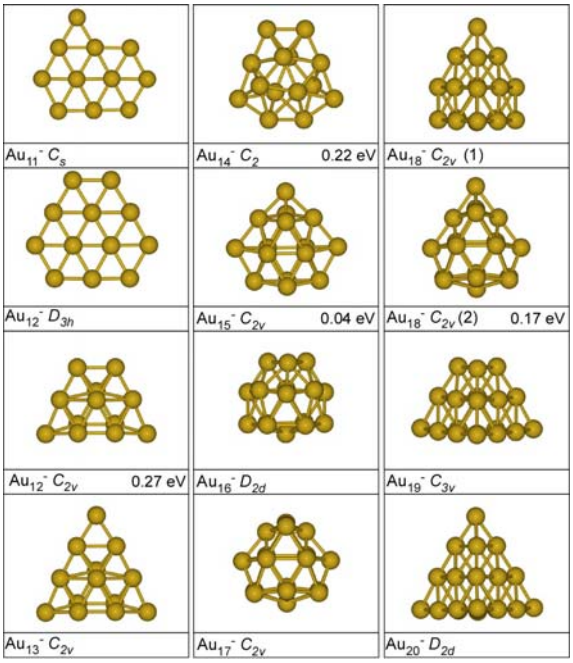

Fig. 4: Structures of gold cluster anions Au_{11}^--Au_{20}^-. Shown are only isomers fitting the TIED data best, together with their point group symmetry. For Au_{12}^- and Au_{18}^- a two component mixture was necessary to fit the experimental data. The two components are shown in each case. In cases where the assigned structure is different from the calculated lowest energy structure, their relative energy is given.

Larger gold cluster anions were studied in subsequent TIED work [C4.6:24]. For Au_{14}^- again a 3D structure fits the experimental data best. Interestingly, this structure is 0.22 eV above the predicted lowest energy isomer, which is again a 2D structure. For Au_{15}^- a flat layered 3D structure closely related to the Au_{14}^- structure is found. At a size of 16 atoms the structural motif changes again: in agreement with theoretical prediction the best fitting structure is a (slightly Jahn Teller distorted) tetrahedral cage structure. Au_{17}^- and the major component of Au_{18}^- are cage structures as well. The lowest energy structure for Au_{18}^-, a fcc-like tetrahedral structure, is the minor component. Finally Au_{19}^- and Au_{20}^- were found to adopt tetrahedral structures.

In most cases the structure predicted by theory (DFT) agrees well with the structure found in the experiments. Significant deviation of experiment and theory were found for Au_{11}-, Au_{14}^- and Au_{18}^-. The lowest energy structures predicted by theory for Au_{12}^- and Au_{14}^- are flat 2D structures. These structures are, however, not found to be dominant in the experiment. For the smaller clusters (Au_{12}^- and Au_{14}^-) extensive structure searches by *ab initio* molecular dynamic and genetic algorithm based methods have been conducted, but no lower energy isomers have been found. The effect of the finite experimental temperature has been tested by free energy calculations in the harmonic approximation. These corrections turn out to be on the order of ~0.01 eV for Au_{12}^-, much smaller than the observed deviation. Additionally, the TIED experiment probes the clusters structure on a timescale of seconds. It is therefore unlikely that the isomer distribution is dominated by meta-stable species. This leaves systematic error in theory as likely explanation for the observed discrepancies. The predicted ground states for Au_{11}^-, Au_{14}^- and Au_{18}^- are planar and tetrahedral, respectively. Both motifs comprise large segments of the gold (111) surface. Clusters containing this structural element seem to be overestimated in stability by standard DFT calculations.

We have acquired TIED data for gold cluster anions with up to 92 atoms. However, due to problems with finding adequate structural models from theory (which become more severe with increasing cluster size) the largest gold cluster which we have been able to assign a structure to so far is Au_{34}^- [C4.6:9]. For this cluster size we find a chiral C_3 structure, in agreement with the lowest energy structure predicted from theory. In addition to the TIED data, photoelectron spectra (PES) were simulated by time dependant density functional theory calculations and compared to experimental PES. In both experiments the C_3 structure gives the best agreement among the model structures considered.

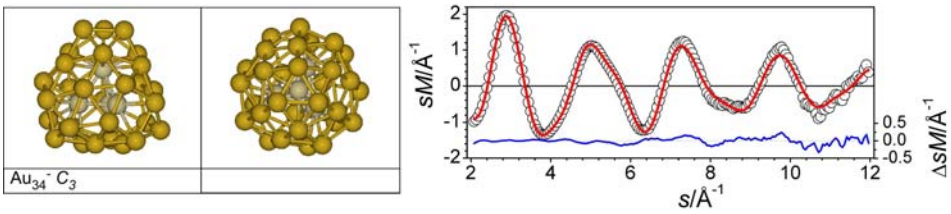

Fig. 5: Left: Lowest energy structure for Au_{34}^- (side and top view). The structure comprises a slightly distorted tetrahedron (lighter atoms) and a reconstructed fcc surface [C4.6:9].

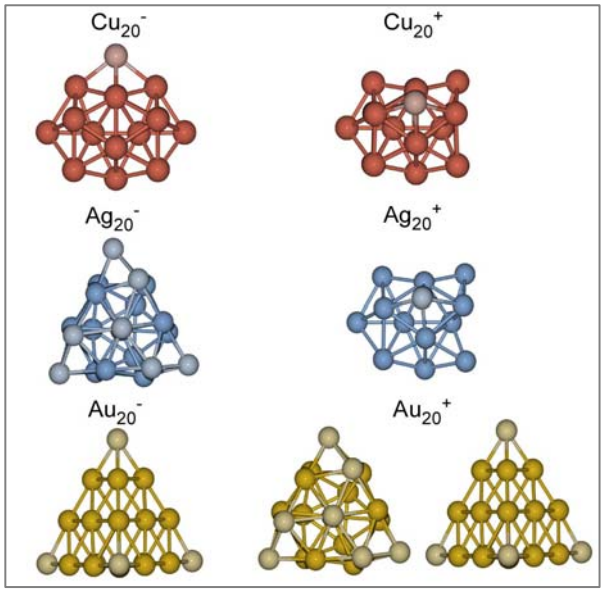

Figure 6: Structures of the coinage metal icosamers cluster ions. For Au_{20}^+ a mixture of structures was found [C4.6:22].

The influence of metal type and charge state on the structure of metal clusters has been studied for the specific case of the three coinage metal icosamers $Cu_{20}^{+/-}$, $Ag_{20}^{+/-}$ and $Au_{20}^{+/-}$ [C4.6:22]. Using TIED in combination with density functional structure calculations we found distinct structural differences depending on the cluster material and the charge state: $Cu_{20}^{+/-}$ as well as Ag_{20}^+ adopt iscosahedral structures. For Ag_{20}^- a distorted icosahedral structure is found. Au_{20}^- as described above is a (slightly distorted) tetrahedron. The experimental data for Au_{20}^+, however, can only be described satisfactorily by a mixture of two isomers with different motifs, a distorted iscosahedral and tetrahedral structure.

As already pointed out in previous theoretical work [5,6] structures of Cu- and Ag-clusters are quite similar (icosahedral), whereas Au clusters prefers non compact structures. The reason for this behaviour can be traced back to the possibility of s-d hybridisation in Au, caused by relativistic effects. In contrast, for Cu and Ag the corresponding effects are much weaker. The degree of s-d hybridisation depends also on the actual structural motif. For some gold clusters this results in relative stabilisation of planar or tetrahedral structures (compensating lower coordination numbers).

The minimum energy structures for a given cluster size are found to be strongly charge dependent, i.e. the relative energetic orders vary while the structures themselves turn out to not change significantly upon positive or negative charging. This can be rationalized if one takes into account, that the clusters still have a significant geometry dependant HOMO-LUMO gap, such that ionisation potentials and electron affinities are distinct for different isomers. Only for larger clusters for which the band gaps approaches zero, does the energetic ordering of the isomers no longer depend on the charge state.

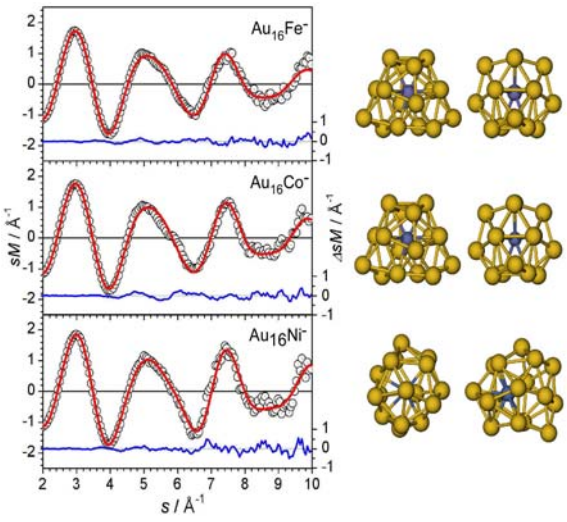

Fig. 7: Best fitting structures of $Au_{16}M^-$, M = Fe, Co and Ni (right, two views rotated by 90°) and the corresponding experimental (open circles) and simulated (red line) modified molecular scattering functions.

Doped gold clusters

As shown above, Au_{16}^- has a cage structure. It possesses a sizable hollow of 5.1Å in diameter, in principle large enough to accommodate a dopant atom. We have investigated Au_{16}^- doped with

magnetic atoms Fe, Co and Ni using TIED in combination with PES and density functional theory [C4.6:26]. We found that the best agreement with experiment is indeed obtained for endohedral structures, but with considerable distortion of the D_{2d} parent cluster Au_{16}^-. For $Au_{16}Fe^-$ and $Au_{16}Co^-$ structures with C_2 symmetry as the major component fit the data best. Interestingly, the C_2 cage structure was found as a higher lying isomer for Au_{16}^-, but was not realized for the pure cluster. For $Au_{16}Ni^-$, a significantly distorted structure is obtained and the position of the Ni-atom is not in the center of the cage in contrast to $Au_{16}Fe^-$ and $Au_{16}Co^-$.

The above TIED structure determinations have also been complemented by comparison between experimental and simulated PE spectra. The spectra of $Au_{16}Fe^-$ and $Au_{16}Co^-$ are quite similar, whereas the spectrum of $Au_{16}Ni^-$ is much more complicated, indicating a different geometrical structure consistent with the TIED assignments.

The bonding situation in these doped systems was inferred from a Mulliken spin density analysis: they can be viewed as Au_{16}^{3-} interacting with Fe^{2+}/Co^{2+}, resp. Au_{16}^{2-} interacting with a Ni^+ ion [C4.6:26]. Even though there is considerable interaction between the impurity atoms and the host cage, the d-states of the dopant atoms are largely localized and in fact their atomic-like magnetism is maintained.

Mixed Gold-Silver clusters $Au_nAg_m^+$ (n+m= 4,5,and 6)

Having studied the ion chemistry of pure gold cluster cations with CO previously over a fairly large size range (< Au_{65}^+) [7] it was of interest to investigate mixed gold-silver clusters as a prototype of a fully miscible alloy. The idea was to understand the influence of local charge density (i.e. at the site of absorption) on the bond strength. Therefore, next to the size dependence, it was interesting to probe the reactivity as a function of composition. Recent photoelectron studies by Negishi et al. [8] on silver-gold cluster anions with sizes up to the five atoms indicate an increase of electron binding energy with gold content. Extensive DFT studies on cationic $Au_nAg_m^+$ (n+m<6) indicate an inhomogenous charge density reflecting significant electron transfer from the silver to the more electronegative gold atoms in the cluster. Similarly, previous IMS probes had already suggested that mixed gold-silver clusters can have significant ionic bonding character [9].

Cluster cations $Au_nAg_m^+$ show a "simple" adsorption reaction with carbon monoxide for cluster sizes starting from the penta-atomic. Note that under our experimental conditions smaller sizes like the tetra-atomic undergo fragmentation with distinctly composition-dependent dissociation channels. While $Au_2Ag_2^+$ looses a silver atom Au_3Ag^+ reacts with CO under loss of a gold atom to yield the triatomic carbonyl. Computations of the reaction pathways indicate that CO adsorption onto $Au_2Ag_2^+$ proceeds via sampling a large number of structural isomers due to the comparatively high binding energy released and small associated interconversion barriers.

For m+n=5 and 6, detailed adsorption kinetic data were determined and rate constants were analyzed to yield binding energies of CO to the metal cluster cation [C4.6:6]. The results indicate that carbon monoxide always binds in an atop position on a single gold atom with a binding energy that generally decreases with increasing number of neighbouring silver atoms (see Fig. 8) [C4.6:21]. This can be understood by the increased charge density on the gold atoms due to their higher electronegativity (relative to silver) and thereby weakening of the σ-donor bond of carbon monoxide.

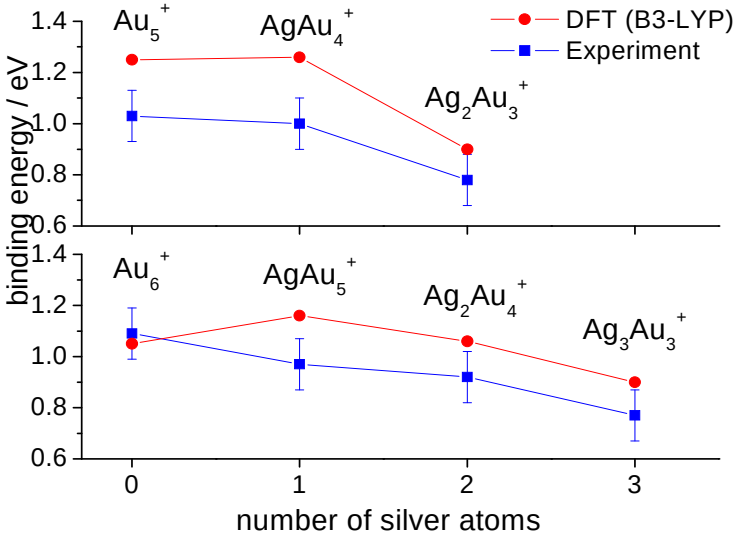

Fig. 8: CO binding energies to $Au_nAg_m^+$ (m+n=5, top panel and m+n=6, bottom panel). Shown are the experimental results from radiative association kinetics (blue) and computational values based on ground state structures (red).

1.4. Boron clusters [C4.6:13]

Inspired by our studies of stable non-IPR fullerene films (C_{58}, C_{56},...; see below), the question came up whether boron, the neighbour of carbon in the periodic table might also manifest "fullerene" like cluster structures. Interestingly, the known bulk phase modification of boron contains a B_{12}-icoahedron as the central building block. It is however strongly covalently bound to neighbouring boron atoms. Further motivation for this research came from a recent publication by Ciuparu et al. [10] who reported the preparation of single-walled boron nanotubes. On the other hand, photoelectron studies by Wang and coworkers [11] suggested planar, sheet-like structures up to n=20. Combining these two observations would imply a transition from planar to cylindrical structures as function of cluster size. Apart from the photoelectron studies, there was only very little experimental information on boron clusters. In particular the structures of boron cluster cations were basically unknown. We therefore decided to shed some more light onto this issue by applying the well-established method of ion mobility spectrometry in combination with density-functional calculations. In the case of boron clusters, the central problem we had to face was the occurrence of a large number of local minima that are very close in energy. In some cases, like for example B_{14}^+, B_{16}^+, and B_{19}^+, even completely different topologies are quasi-degenerate in energy. The lowest energy isomer of B_{14}^+ for example is essentially planar, the second-best structure, a nanocylinder of fused B_3-triangles is only 0.08 eV higher in energy. To complicate things further, some of the geometries we found as local minima are completely unexpected, i.e. they can hardly be obtained by chemical intuition. Therefore many local minima or even the global minimum can be easily missed unless an unbiased search is performed. We solved this problem by using a genetic algorithm. As a result, we obtained a list of different local minimum structures with their corresponding relative energies. We compared the collision cross sections of all energetically reasonable candidate structures with the experimental value. As a result, we found that cationic boron clusters are planar up to B_{15}^+, starting at B_{16}^+ we find nanocyclinders. Icosahedral structures, prominent in bulk phase boron, are completely absent. We see a tendency towards cylinders with more than two boron ring segments, i.e. towards single-walled nanotubes, and we plan to deposit boron cluster ions under soft landing conditions in the near future in order to probe resulting materials.

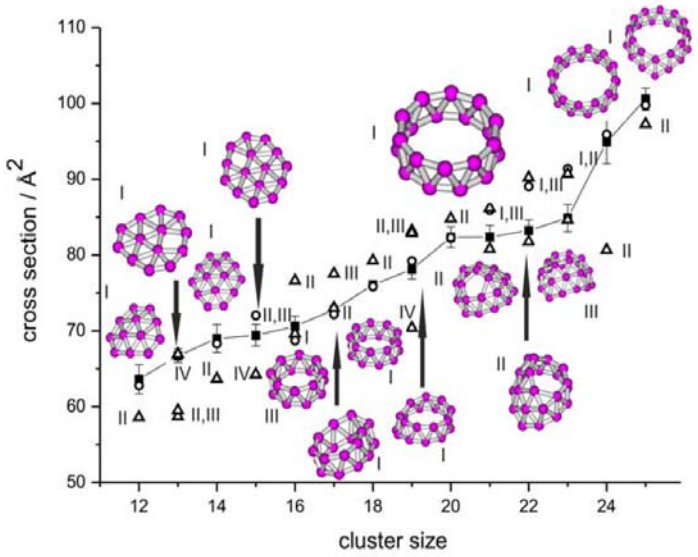

Fig. 9. Boron cluster cations: comparison of calculated and experimental cross sections. The squares (■) and error bars correspond to the experimental values. The line connects the experimental values. Open circles (○) correspond to the calculated global minima, open triangles (Δ) to structures higher in energy

1.5. Tin clusters [C4.6:25], [C4.6:28], [C4.6:31]

Tin is another promising candidate for cluster assembled nanomaterials since the binding energies of tin clusters quickly converge towards the bulk value [12]. Based on photoelectron measurements and quantum chemical calculations Wang and coworkers [13] concluded that Sn_{12}^{2-} is a perfectly icosahedral, stable cage and suggested that "it may be synthesized in solid state using suitable ligands or counterions". There is however no direct structural information on these clusters in gas phase. We determined the structures of positively and negatively charged tin clusters by IMS and TIED and found an icosahedral cage structure for Sn_{12}^{-} and prolate structures for the larger tin clusters.

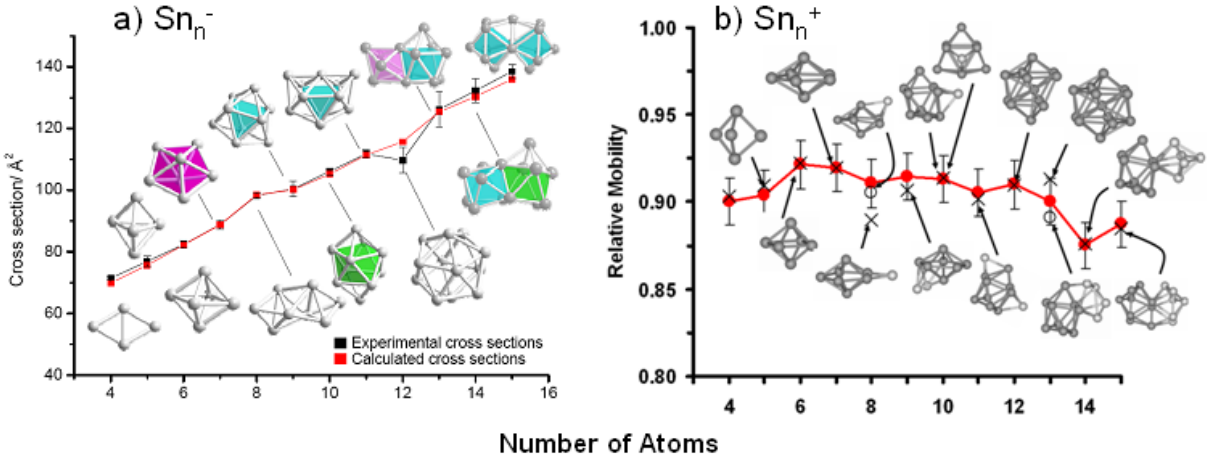

Fig. 10: a) Comparison of calculated and experimental cross sections for tin cluster anions: common structural features found for many different cluster sizes are pentagonal bipyramids (purple), trigonal prisms (blue) and tetragonal antiprisms (green). Sn_{12}^{-} is however (quasi) icosahedral. b) Relative mobilities and structures for tin cluster cations.

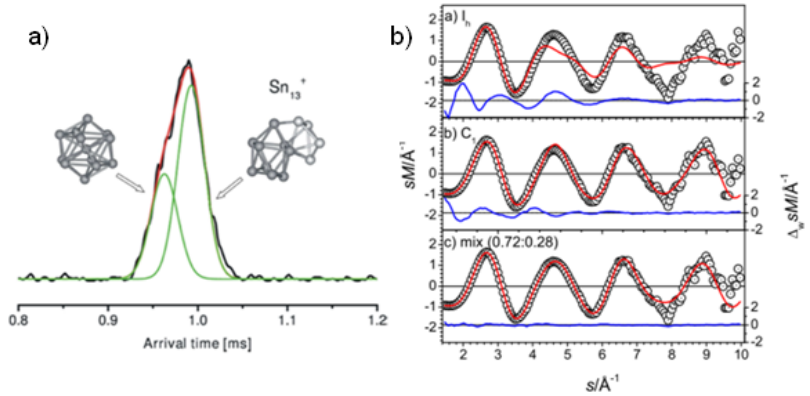

Fig. 11: a) Arrival time distributions (ATDs) as determined by IMS measurements for Sn_{13}^+. Sn_{13}^+ has an exceptionally wide ATD (t ≈ 55µs) indicating a multi-isomer superposition. b) TIED measurement of Sn_{13}^+. The measured diffration data can only be explained by a multi-isomer superposition consistent with the IMS measurement.

For Sn_{13}^+ we find two isomers, both in the IMS and the TIED measurements.

The stability of tin clusters has been directly probed by collision induced dissociation, i.e. by injecting a particular cluster mass into the drift cell and scanning the fragment distribution. We observe a transition in the fragmentation pattern from predominantly atom and dimer loss for the small clusters ($Sn_{11}^{+/-}$ and smaller) to fission-type fragmentation for the larger clusters - especially Sn_7^- and Sn_{10}^- loss is very prominent. This is in line with the calculated fragmentation energies for the different channels. A promising candidate for soft landing deposition is Sn_{14}^-: It fragments easily, but the only fragmentation products are the very stable Sn_7^- clusters, which may perhaps be further stabilized on a surface by weakly bound ligands.

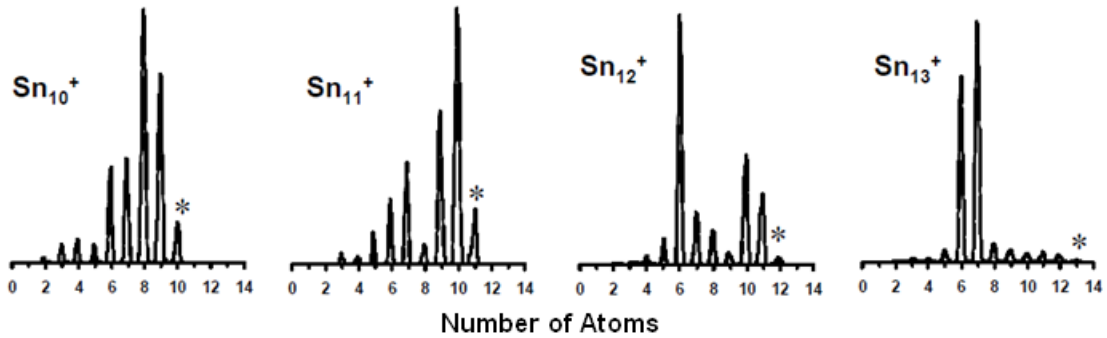

Fig. 12: CID mass spectra of Sn_{10}^+, Sn_{11}^+, Sn_{12}^+, and Sn_{13}^+. The star indicates the unfragmented parent ion. Note the change in fragmentation pattern from sequential atom loss to fission between Sn_{10}^+ and the larger clusters.

Larger tin cluster anions Sn_n^- n = 18, 20, 23, 25 have been studied by TIED. These clusters comprise dimers of the stable subunits. The lowest energy structure for Sn_{18}^- comprises two interlinked Sn_9 tricapped trigonal prisms (ttp) in full agreement with the TIED data. The tentative ground state of Sn_{20}^- consists of two bicapped ten atom tetragonal anti-prisms (bta). The next higher lying isomer differs only in the relative orientation of bta units. Both isomers are able to fit the

experimental data, however, structures with a different motif can be ruled out. In Sn_{23}^- two bta units are connected by three bridging atoms. Also Sn_{25}^- is composed of two discrete clusters: a 10 atom bta and a 15-atom cluster. Interestingly the 15-atom subunit strongly resembles the ground state structure of Sn_{15}^- (see above). Again several low energy structures were found, which differ only in the relative orientations of their component clusters. They are close in energy and fit the experimental data likewise. However structures deviating from the 10+15 motif can be ruled out. In summary we observe a common structural motif in this size regime: segmented chains of discrete Sn_n subunits of particularly high stability.

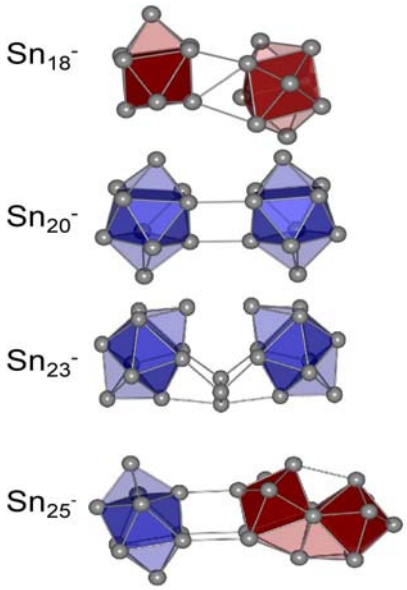

Fig. 13: Lowest energy structures of Sn_{18}^-, Sn_{20}^-, Sn_{23}^- and Sn_{25}^- comprising dimers of the stable subunits tricapped trigonal prism (red) and bicapped tetragonal anti-prism (blue).

1.6. Lead clusters [C4.6:32]

Lead clusters are in some respects similar to tin: Pb_7^+ and Pb_{10}^+ are very abundant in the cluster ion beam while Pb_{14}^+ is of much lower intensity [14]. Based on photoelectron measurements [15,16,17,18,19] it has been assumed that Pb_{12}^- - like Sn_{12}^- - has a highly symmetric icosahedral structure. On the other hand, ion mobility measurements [20] (on cations only) had indicated that lead prefers more compact structures than tin (without exact structural assignment). We combined ion mobility measurements and relativistic (scalar+spin-orbit-coupling) DFT calculations to assign structures of both lead cluster cations and anions up to 15 atoms. Up to $Pb_7^{+/-}$ we find basically the same structures as for tin, independent of charge state, with Pb_6^+ (fused tetrahedra instead of octahedron) as the only exception. For the larger clusters we always find different structures for cations and anions. For example, Pb_{12}^- is confirmed to be a *hollow* icosahedron while Pb_{12}^+ is a truncated *filled* icosahedron. Pb_{13}^+ is a *filled* icosahedron but Pb_{13}^- is a *hollow* icosahedron with the additional atom capping a face. In comparison to tin, the larger clusters are significantly more compact.

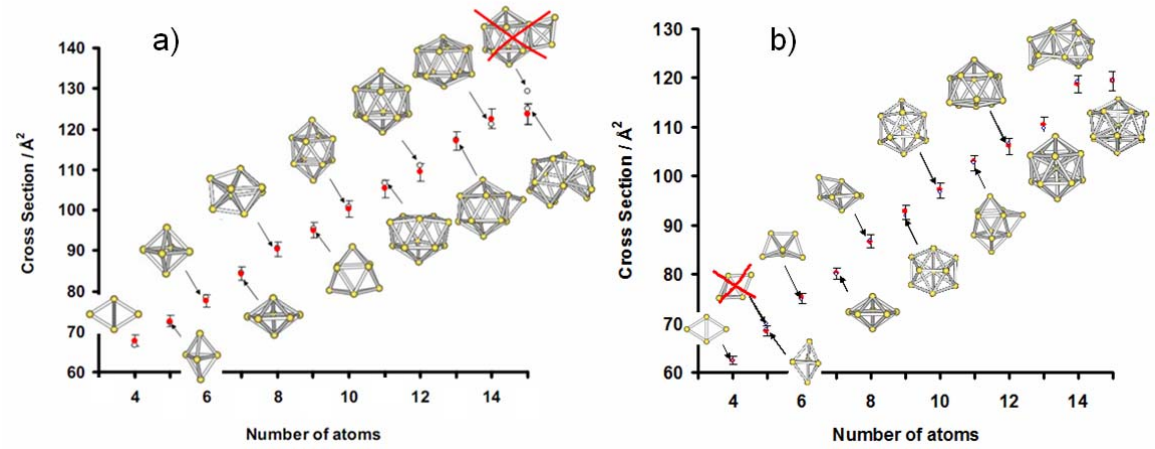

Fig. 14: Collision cross sections of lead cluster anions (a) and cations (b) as a function of cluster size. Experimental values: full red circles and error bars. Theoretical values: open circles.

In order to get information on the relative stabilities, we investigated the collision induced dissociation mass spectra for the different cluster sizes and charge states, and observed a strong correlation with the calculated fragmentation energies. Up to n=13 the main fragmentation channel is atom loss, for the larger cluster sizes we observe - as for tin - fission into large fragments. This channel is dominant for larger anions, less pronounced but clearly also present for the cations.

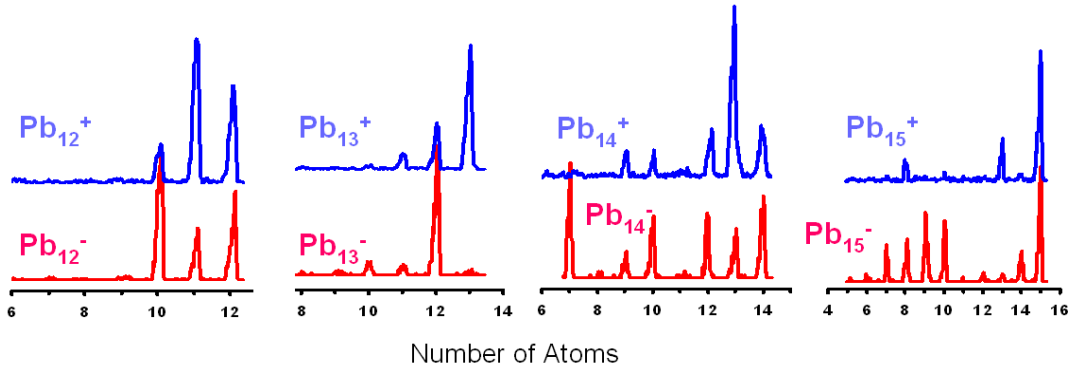

Fig. 15: Fragmentation mass spectra for the larger lead clusters. Note the change in fragmentation pattern from sequential atom loss to fission

2. Support Interactions and Thermal Stability of Size Selected Clusters Deposited onto Single-Crystal Surfaces

At the beginning of the past project period we had established that it is possible to prepare novel solid materials consisting of mass selected non-IPR (=non isolated pentagon ring) fullerene cages: C_{50}, C_{52}, C_{54}, C_{56} and C_{58} [21] by ion beam soft-landing onto inert surfaces. The corresponding C_n cages were generated by electron impact induced ionization, thermal excitation and subsequent fragmentation of IPR C_{60} fullerenes, $C_{60} \rightarrow C_{58} + C_2 \rightarrow C_{56} + C_2 \rightarrow \ldots \rightarrow C_{48} + C_2$. Preliminary characterization provided evidence that non-IPR fullerene films comprised interlinked cluster materials which could be thermally back-transformed into component building blocks. The covalent interlinks were determined to take the form of bonds between reactive non-IPR sites on adjacent cages. During the past project period we have characterised the stability and reactivity of these novel C_n films and have compared their properties to those of IPR fullerene solids.

2.1. Formation and thermal stability of cesium fullerides

First, we have studied the relative ability of IPR vs. non-IPR C_n films to form fullerides. This choice was motivated by the superconductivity found for alkali-metal doped IPR C_n films [22]. Thermal stability, sublimation properties and the surface topography of C_{60} cesium fulleride films (Cs_xC_{60}) were studied using samples prepared by exposing HOPG, to calibrated effusive C_{60} and Cs fluxes. The results obtained (thermal desorption spectra with mass spectrometric detection of all desorbing species) were related to the electronic properties of the same films as determined by ultraviolet- and x-ray photoelectron spectroscopy. The surface topography of the Cs_xC_{60} solids was studied by scanning electron microscopy, SEM, and scanning force microscopies, AFM.

Cs doping of C_{60} films at room temperature proceeds via the spontaneous formation of a Cs_xC_{60} phase(s). Weakly doped films, $Cs_{x<4}C_{60}$, undergo thermally induced decomposition which manifests itself via three well distinguishable C_{60} sublimation peaks: α at 570 K, β at 660–720 K, and γ at 820–930 K. Peak α corresponds to C_{60} desorption from pure C_{60} regions. Sublimation peak β is associated with desorption of more strongly bound C_{60} from layers terminating Cs_xC_{60} phases $0<x<4$. The ensuing saturated Cs_xC_{60}, $4<x<6$, phases decompose only via the sublimation of intact Cs_xC_{60} molecules. The related sublimation band γ marks the limit of the thermal stability of these phases. Its maximum shifts to higher temperature with increasing Cs doping degree, $820\ \text{K} < T < 930\ \text{K}$. SEM images (see Fig. 16) of weakly doped films indicate spontaneous formation of nm-sized fulleride grains upon room temperature deposition and as such provide evidence for a segregation process associated with Cs doping. There are interesting parallels to the elementary processes considered in a recent theoretical treatment of dewetting [24]. Analogous experiments have been performed by cesium doping non-IPR fullerene films. Significantly different thermal desorption phenomena are observed relative to IPR fullerene results. In the case of non-IPR C_{58} cesium doping (and associated charge transfer) facilitates a thermally-induced disproportionation reaction leading to C_{56} and C_{60} products.

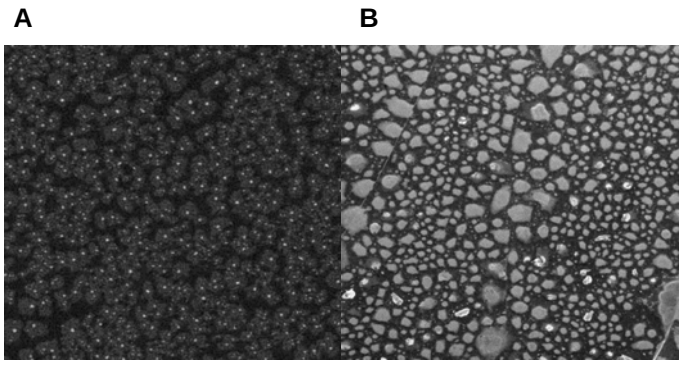

Fig. 16: SEM images showing changes to the surface topography of a 20 MLE thick C_{60} film upon increasing Cs doping: (A). weakly doped Cs_xC_{60} film of nominal composition $x<1$, and (B). highly doped Cs_xC_{60} phase, $x>4$. The bright areas indicate nanophase segregation and are attributed to grains of higher cesium content. Taken from [C4.6:17].

2.2. Properties of Deuterofullerenes

In the context of hydrogen storeage media, we have investigated the hydrogenation of IPR fullerene films (C_{60} and C_{70} films). Previous literature studies of fullerene to fullerene hydride conversions have shown that highest hydrogen contents are realized by means of metal hydrogenation catalysts which dissociate molecular hydrogen [25]. This yields $C_{60}H_{42}$ and $C_{60}H_{44}$ species (with some traces of $C_{60}H_{52}$) as the final stages of sequential hydrogenation [26]. The fully saturated $C_{60}H_{60}$ species cannot be generated because apparently such high hydrogen loading leads to cage fragmentation. In our study, the reaction was performed by exposing C_{60} films predeposited onto HOPG to a flux of atomic deuterium. The initial stage of *on-top* deuteration at room temperature is associated with the formation of a "capping" layer which exhibits *higher* thermal stability than pristine C_{60} films. Correspondingly, the sublimation temperature T_s as monitored by temperature resolved mass spectroscopy, TRMS, increases linearly with the deuterium dose applied. The related sublimation heat for the capping layer was determined to be 2.15 eV/cage for deuterium exposures in the range of 10^{16} D/cm^{-2}. Capping layers appear to kinetically hinder further deuteration of subsurface C_{60}. This hindrance can be reduced by performing the initial (and subsequent) deuteration at elevated sample temperatures. Further deuterium exposure then leads to the formation of higher deuterofullerenes (e.g., $C_{60}D_{36}$ or $C_{60}D_{44}$), which exhibit *considerably lower* sublimation enthalpies of ~1.4 eV/cage. The same procedures have been applied in a study of C_{70} film deuteration with quite analogous results. The capping layer [$C_{70}D_x$] exhibits higher thermal stability than the higher deuterofullerenes, e.g. $C_{70}D_{36}$.

Capping layers have previously not been reported in the hydrogenation/deuteration of IPR fullerenes and consequently represent a new $C_{IPR}D_x$ phase. The resulting capped films are air-resistant and amenable to the fabrication of stable multilayered $[C_{60}/C_{60}D_x]_m$ structures [C4.6:11]. The molecular structure of the capping layer remains unclear. Conceivably, the formation of localized C-D bonds on individual C_{60} cages facilitates covalent -C-C- bonding *between* adjacent C_{60} cages. The stability of the resulting $[D_xC_{60}]_n$ material might be further enhanced by bridging of adjacent oligomers with interstitial deuterium atoms. Recent ^{2}H and ^{13}C NMR investigations of deuterofullerenes generated by D_2 pressurization of solid C_{60} films to 2.5 MPa have been interpreted in terms of both single C-D and -C-D-C- bridging bonds [27].

In contrast to the *formation* of polymeric fullerene chains upon reaction with atomic hydrogen/deuterium as found here for IPR fullerene films, non-IPR films show intercage bond *cleavage* upon deuterium exposure (and incorporation), i.e. qualitatively different behaviour [C4.6:7]. Whereas deuterated IPR films show an increased sublimation temperature T_s upon low-dose deuteration, all non-IPR C_n films studied exhibit continuous T_s decrease with progressing deuteration [28]. By continuing the exposure, the disconnected C_n cages become terminated by

increasing number of D atoms. This coating of the C_n cage by covalently bound deuterium prevents C-C intercage bonds from being (re)formed and consequently van-der-Waals-like cage-cage interactions ensue. This, picture is supported by corresponding changes to electronic structure as evidenced by valence band UPS, as well by AFM measurements of the surface topography of the deuterated C_n films. Fig. 17 illustrates the opposing trends in the T_s(Dose) function for deuterated C_{60} vs. C_{58} films.

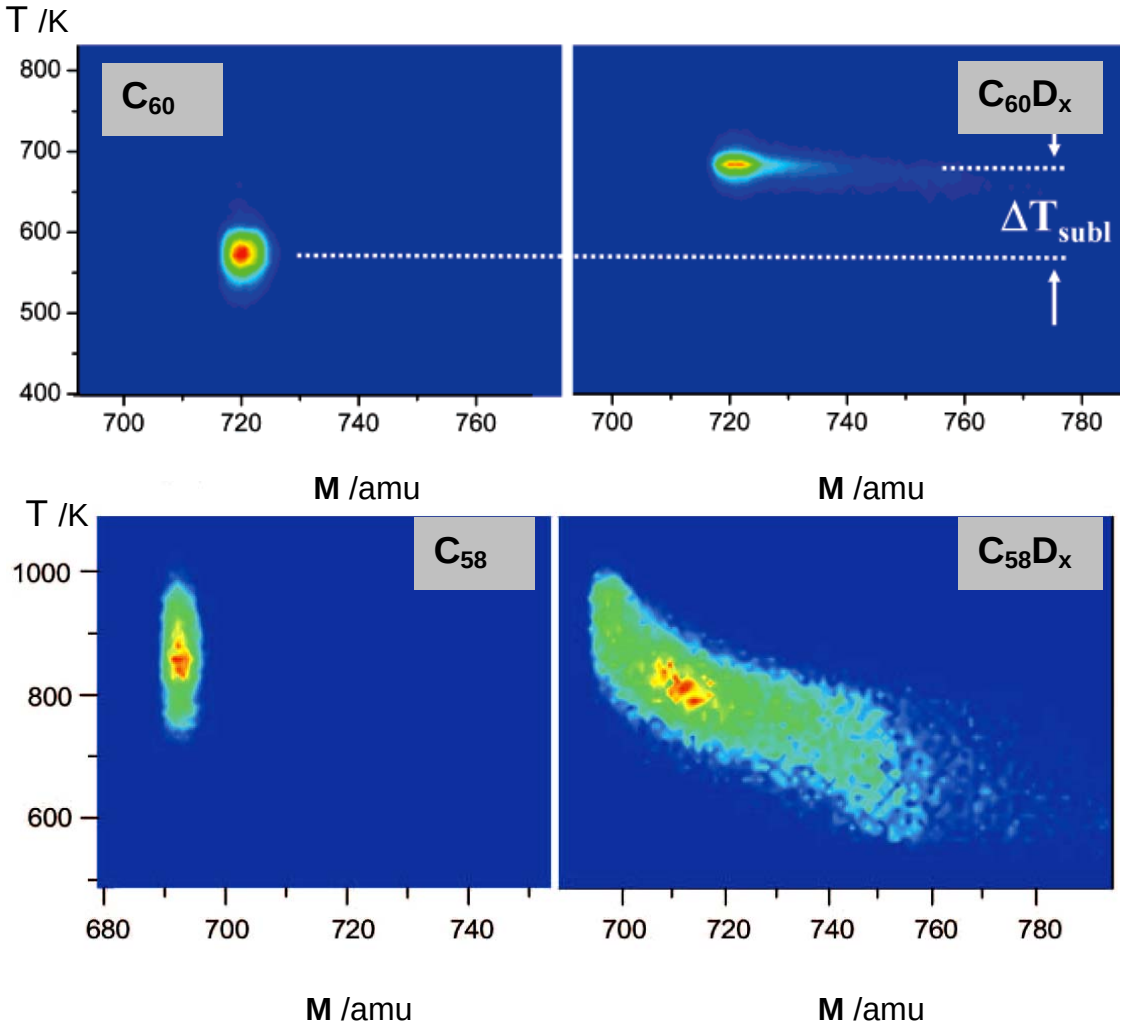

Fig. 17: TRMS maps illustrating the upward shift of the sublimation temperature as observed for deuterated IPR C_{60} fullerene films (upper panel). The TRMS maps in the lower panel illustrate the deuteration-induced lowering of the sublimation temperature as observed for all non-IPR films. The ΔT_{subl} values scale with the deuterium content x. Taken from [C4.6:11] and [C4.6:7].

2.3. Alkali metal activated deuterium release from non-IPR fullerene deuterides

Given the high hydrogen loadings possible, fullerene hydrides would be attractive hydrogen storage systems if dihydrogen could be easily released upon heating to slightly above room temperature. Unfortunately, our mass spectroscopic TDS measurements provided no evidence for the co-desorption of D_2 molecules during $C_{60}D_x$ sublimation (up to 1000 K). Only a broad spectrum of the $C_{60}D_x$ deuterofullerenes was identified. On the other hand, alkali metals are known to activate various elementary reactions (e.g. ammonia synthesis) as a result of bond weakening due to electron

transfer. Thus, we have explored the use of Cs atoms as catalysts for D_2 release from deuterofullerenes – by probing for D_2 emission upon heating Cs-doped deuterofullerene films, $Cs_x(C_{60}D_n)$, and relating these observations to changes in electronic structure and composition of the samples [C4.6:20]. Mass spectra taken during sublimation indicate that deuterofullerene ($C_{60}D_n$) and fullerides Cs_xC_{60} can coexist at elevated temperatures. The yield of Cs fulleride phases obtained by heating increases with the amount of Cs atoms initially deposited/intercalated into the deuterofullerene thin films. At highest initial Cs doses, a Cs_xC_{60} phase with doping degree of $4 < x < 6$ is eventually generated. UP spectra of the ternary $Cs_x(C_{60}D_n)$ films taken before heating suggest that C_{60}-D^{-d}-Cs^{+d} complexes are initially formed. Thermally activated conversion of these complexes into Cs fullerides can be followed by recording UP features characteristic for (increasing) C_{60}-LUMO state occupation. The transition from cesium intercalated $C_{60}D_n$ into Cs_xC_{60} sets in at temperature of ~610 K and is completed at 670 K. This narrow transition temperature range is also characterized by synchronous desorption of Cs ***and*** $\boldsymbol{D_2}$. We conclude that Cs intercalation can significantly weaken >C-D bond strengths relative to $C_{60}D_n$, thus facilitating thermally activated dedeuteration which leads to D_2 emission.

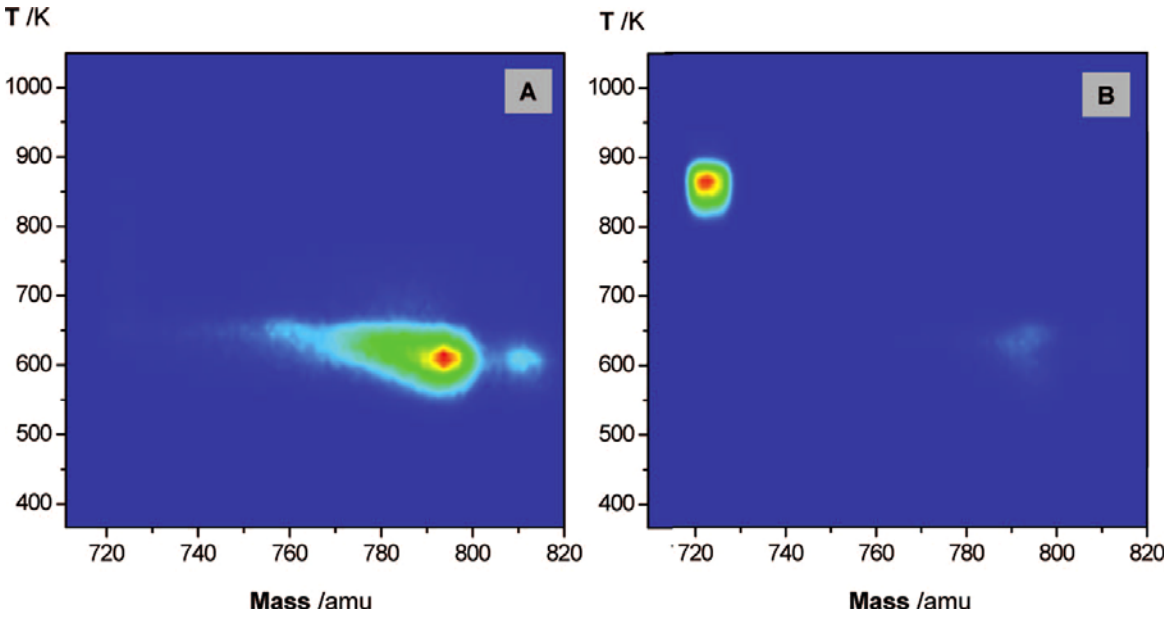

Fig. 18: TRMS maps taken before and after exposing preformed 10 MLE thick deuterofullerene films to a Cs dose of ~1.8×10^{17} atoms, left and right panels, respectively. Both the deuteration procedure as well as the Cs deposition were performed at 475 K. Taken from [C4.6:20].

2.4. Non-IPR C_{60} solids

As mentioned in the introduction to this section, small non-IPR cages (C_{58}, C_{56}, C_{54}, C_{52} and C_{50}) were generated by electron-impact induced fragmentation of IPR-C_{60} cages [29]. In the second part of the project period we extended the spectrum of available non-IPR C_n cages by fragmenting IPR-C_{70} to form C_{68}, C_{66}, C_{64}, C_{62} and $\boldsymbol{C_{60}}$ cages. This led us to explore the question whether the C_{60} fragment cages generated from C_{70}, might have different molecular structures than the well known IPR C_{60} isomer, $C_{60}(I_h)$ [C4.6:27]. For this purpose, we first produced monodisperse films by depositing vibronically excited C_{60}^+ ions generated from C_{70} onto HOPG. Mass resolved TDS

measurements on these films showed a major desorption peak corresponding to $C_{60}(I_h)$ but also a significant desorption tail to higher temperatures indicating that less volatile C_{60}^* isomeric species (ca. 10%) were also present in the deposit. This also implied that the major IPR C_{60} component could be selectively removed simply by heating the film up to ~600 K which results in the thermal desorption of $C_{60}(I_h)$. The topography of the resulting residue films, as studied by means of AFM, strongly resembles that observed for (other) non-IPR cages. This in turn suggests that C_{60}* can aggregate by way of forming of covalent intercage bonds. These intercage bonds are responsible for the high stability of the C_{60}* films as mirrored by the considerably higher sublimation temperature (~1100 K) than observed for $C_{60}(I_h)$. The density of states in the valence band of the C_{60}* material also exhibits a different structure. In contrast to the characteristic doublet of the HOMO-derived band of C_{60} (I_h) films, entiched C_{60}* films exhibit a HOMO-triplet with a well distinguishable additional peak at a binding energy of ~2.6 eV. This is an indicator of the electronic modifications induced by quasi-covalent intercage bonds. C_{60}* films exhibit a narrower HOMO-LUMO gap than found for $C_{60}(I_h)$. DFT calculations performed for various short oligomers of C_{60} cage isomers show that both the experimentally observed HOMO-band and the enhanced stability of the new films can be well explained by assuming that the C_{60}* material is composed exclusively of the lowest energy non-IPR cage isomer of C_{60}. Such $C_{60}(C_{2v})$ isomers can apparently result from thermally activated Stone-Wales rearrangements within precursor fullerene cages [30]. $C_{60}(C_{2v})$ has two reactive sites constituted by two adjacent pentagonal rings, 2AP and is less stable than $C_{60}(I_h)$ by ~ 1eV.

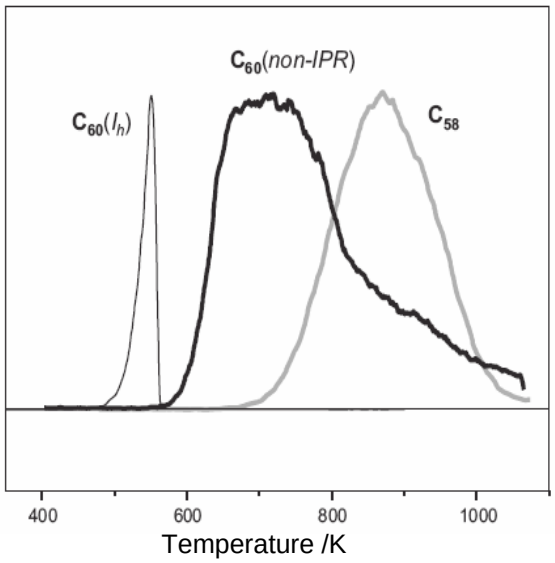

Figure 19: Thermal desorption bands for non-IPR C_{60} cages (thick black curve) in comparison to IPR C_{60} and non-IPR C_{58}, thin and grey curves, respectively. The non-IPR C_{60} material exhibits higher thermal stability than $C_{60}(I_h)$. The intercage bonds constituted by non-IPR reaction centres are responsible for this pronounced stabilization. Taken from [C4.6:27].

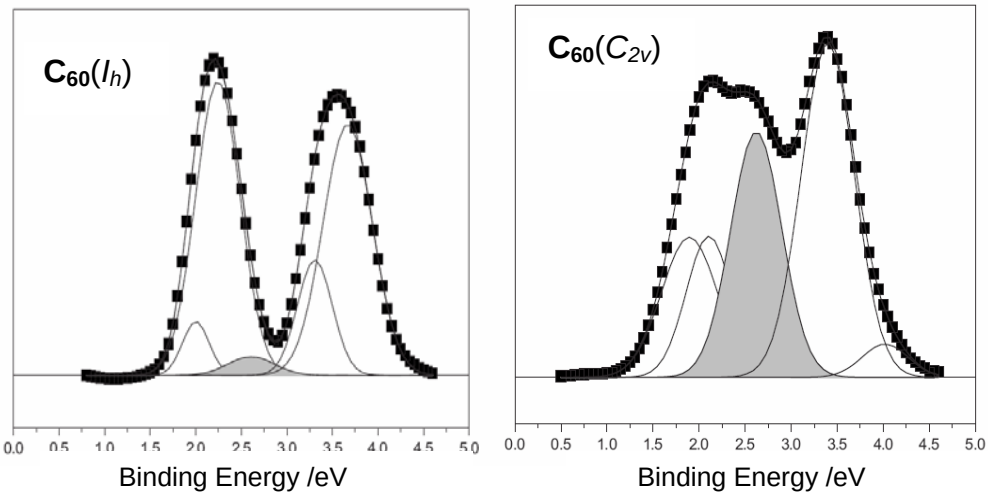

Fig. 20: Valence band UP(21.2 eV) spectra obtained for thick $C_{60}(I_h)$ and $C_{60}(C_{2v})$ films, left and right panels, respectively. The valence band of the IPR material exhibits a characteristic doublet in the HOMO region. In contrast, the HOMO band of the non-IPR material manifests a triplet-like profile. This characteristic DOS profile can be qualitatively reproduced by DFT calculations of covalently interlinked $C_{60}(C_{2v})$. Taken from [C4.6:27]

2.5. New monodisperse materials consisting of non-IPR C_n cages (48<n<70)

Electron-impact induced ionization/fragmentation of C_{70} has also been used to produce a series of monodisperse materials consisting of non-IPR C_n cages (C_{60}<n<C_{70}) via soft landing deposition onto HOPG held at room temperature [C4.6:30]. Whereas the reference IPR fullerene films resulting from deposition of unfragmented C_{60}^+ and C_{70}^+ manifest compact 2D island topographies at submonolayer coverages, all non-IPR fullerene films deposited under the same low energy conditions grow via formation of dendritic C_n aggregates. The latter are stabilized by quasi-covalent intercage bonds as mediated by the non-IPR sites (primarily adjacent pentagon pairs, AP). For each cluster size, a significant fraction of the deposited non-IPR C_n cages can be (re)sublimed by heating. The corresponding mean desorption activation energy, E_{des}, depends on the size of the constituting C_n cages. It increases from 2.1 eV for C_{68} up to 2.6 eV for C_{50}. The densities of states in the valence band regions (DOS), surface ionization potentials (IP) and HOMO-LUMO gaps (Δ) of non-IPR films were found to vary strongly with cage size. [C_{70}]- and [C_{60}]-fragment derived films differ somewhat in their valence-band DOS structure. Whereas [C_{70}]-fragment derived non-IPR films show four ultraviolet photoelectron spectral features, [C_{60}]-fragment derived films manifest only three resolvable features. Surface IP values of non-IPR films range from 6.55 eV to 6.85 eV and are significantly lower than those of parent C_{60} and C_{70} films. Whereas IPR films exhibit Δ values around 2 eV, non-IPR films have Δ values ranging from 0.8 eV to 1.8 eV. C*1s* X-ray photoelectron spectroscopy of non-IPR films reveals a component peaked at 286.3 eV which can be assigned to (interconnected) -2AP sites. In general, dependencies of E_{des}, DOS, IP and Δ on the cage size n can be interpreted in terms of covalently interconnected oligomeric structures *comprising the most stable (neutral) C_n isomers* as determined by density functional theory (DFT) calculations.

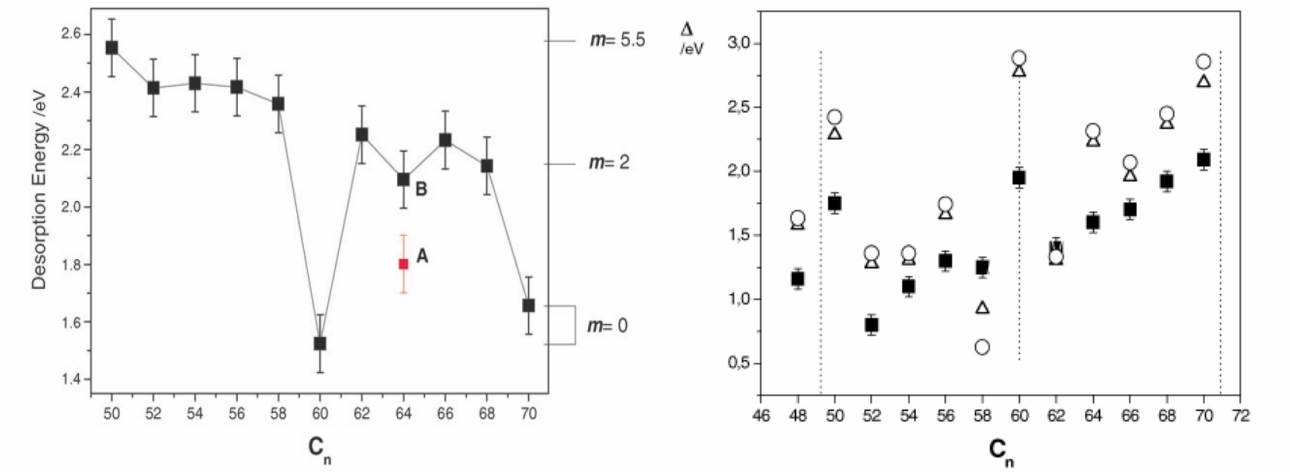

Fig. 21: Left panel illustrates the dependence of the desorption energy, E_{des}, on the nuclearity of the C_n building blocks. $E_{des}(n)$ can be related to the maximum number of intercage bonds which can formed between the non-IPR sites on the respective cages. Specifically, E_{des} values scale with the mean number of such non-IPR sites per cage, m, as predicted by DFT for the most stable C_n cage isomers. Right panel shows the dependence of the HOMO-LUMO gap, Δ, on the size of the constituting C_n cages (black squares). The experimental values obtained for the C_n materials follow the trend predicted by DFT calculations performed for isolated lowest C_n isomers (open circles). Taken from [C4.6:30].

2.6. Energy dissipation during soft-landing of the C_n cages

We systematically studied the influence of the various deposition conditions used (E_0, T_s) on the resulting surface topography of the C_n films created [C4.6:33]. The corresponding deposition experiments were carried out under nominally normal incidence and at hyperthermal incident kinetic energies, E_0 (1-40 eV). Surface temperatures during deposition, T_s, were varied from 300 K to the desorption onset of ~700 K. Initial sticking of C_n cages is governed by the lateral density of step edges, which act as pinning and nucleation centres for migrating cages. Consequently, in the early deposition stages, the surface exhibits large areas of empty terraces, while the step edges themselves are well-decorated. The terraces in turn become decorated by dendritic C_n islands in later deposition stages. The mean size of these 2D islands and the mean distance between nearest islands, δ, scale with the size of the terraces (step-step distance). When increasing E_0, the fractal-like islands become smaller and less dendritic in shape. The mean initial sticking coefficient decays exponentially with increasing E_0. The island topography has also been found to depend sensitively on T_s. Instead of the dendritic/fractal islands generated at room temperature, densely packed islands terminated by smooth rims are observed upon deposition at elevated temperatures. The findings have been rationalized in terms of a three step deposition process involving: (i) conversion of perpendicular E_0 into hyperthermal surface parallel gliding/sliding motion, (ii) friction–dissipation of this surface-parallel kinetic energy within an (unexpectedly large) mean free path Λ followed by (iii) thermal diffusion. Λ, is observed to scale with E_0 and T_s. By modelling the data by simple analytical formula including all three loss components the mean friction coefficient for a C_n cage sliding across the terraces has been determined: $\eta = 8400$ eVs/m^2.

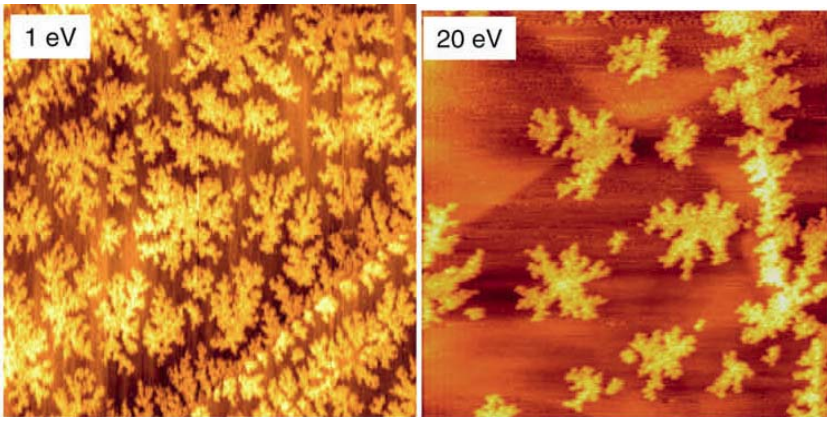

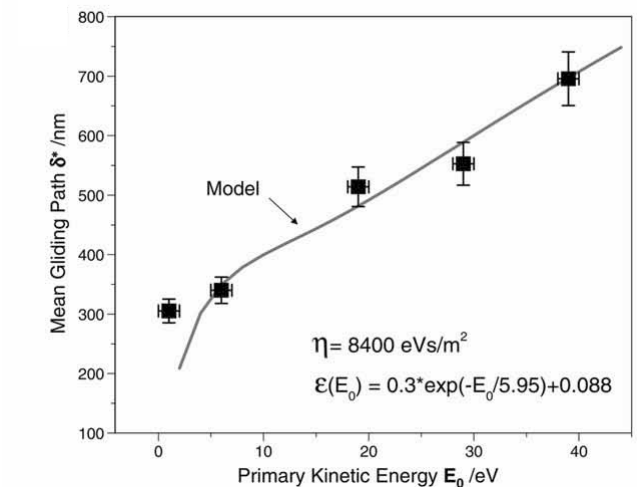

Fig. 22: Upper panel shows two AFM images (1.5 x 1.5 μm) of the C_{58} deposits illustrating the role of the incident kinetic energy on island growth. Lower panel shows the mean distance between adjacent islands, Λ, as a function of E_0 (black squares). The data were fitted by a model which relates the mean gliding path to the energy dissipation in the sliding event (grey curve). Taken from [C4.6:33].

2.7. High resolution microscopy of soft-landed clusters

In cooperation with C4.5 we have studied the structural properties of mass selected transition metal clusters deposited onto amorphous carbon using high resolution transmission electron microscopy, HRTEM - concentrating primarily on gold (and tin) clusters. We refer the interested reader to the corresponding C4.5 project report and to the resulting joint publications [C4.6:16] [C4.6:23]. In cooperation with C4.10 we have also begun to apply liquid helium temperature UHV-STM to study non-IPR fullerene deposits at submonolayer coverages on a variety of substrates – notably natural graphite and single-crystalline copper. For these experiments, samples are transferred between the respective machines while maintaining high vacuum conditions (using a corresponding battery-powered transfer-chamber setup, appropriate load locks and sample manipulators). Initial results are encouraging and suggest that it will be possible to determine cage structures via atomic resolution images thus providing for direct isomer differentiation. For a more detailed summary of these results the reader is again referred to the corresponding project report.

In a recent development we have implemented in-situ Raman and surface-enhanced Raman (SERS) microscopies (20 micron spot size; 785 nm excitation) to probe the vibrational/phonon spectra of deposits generated by ion beam soft-landing. SERS measurements are performed using commercial Klarite™ substrates (periodically microstructured gold) onto which we have so far deposited: (i) mass selected non-IPR fullerene cations as well as (ii) two component layers comprising fullerene cations alternating with small carbon cluster anions (e.g. $C_{58}^+ + C_2^-$) in order to probe the corresponding thermally activated cage insertion chemistry.

3. Ongoing method development

We are close to completing the construction of a second ion beam soft-landing apparatus, which we hope will find extensive application in the next CFN project period. This machine comprises an electrospray ion source, quadrupole filter mass selection and a deposition chamber equipped with a liquid helium cooled soft-landing target - also compatible with co-deposition of (neutralized) ions into inert gas matrices. Various spectroscopic analysis methods including infrared reflection/absorption spectroscopy (IRAS), (low frequency) Raman, SERS and visible fluorescence will be implemented.

Also worth mentioning in this context is our recent successful development (in a separately funded project) of an apparatus which combines a high throughput ion mobility stage (HT-IMS) for efficient isomer/conformer separation with a photoelectron spectrometer [31]. Our experience with the electrospray source on this machine shows that 50% of the ions generated can be transmitted using an HT-IMS stage while also providing for isomer selection. This would allow for mass *and isomer* selected soft-landing deposition studies in future.

References

- for references to CFN funded work during project period (cited as [C4.6:xx] above), see separate subproject publication list -

[1] D. Schooss, M. N. Blom, J. H. Parks, B. von Issendorff, H. Haberland, and M. M. Kappes, Nano Lett. 5 (10), 1972 (2005).
[2] F. Furche, R. Ahlrichs, P. Weis, C. Jacob, S. Gilb, T. Bierweiler, and M. M. Kappes, J. Chem. Phys. 117 (15), 6982 (2002).
[3] H. Häkkinen, B. Yoon, U. Landman, X. Li, H. J. Zhai, and L. S. Wang, J. Phys. Chem. A 107 (32), 6168 (2003); X. Xing, B. Yoon, U. Landman, and J. H. Parks, Phys. Rev. B 74 (16), 165423 (2006).
[4] P. Koskinen, H. Häkkinen, B. Huber, B. von Issendorff, and M. Moseler, Phys. Rev. Lett. 98 (1), 015701 (2007).
[5] H. Häkkinen, M. Moseler, and U. Landman, Phys. Rev. Lett. 89 (3), 33401 (2002).
[6] E. M. Fernandez, J. M. Soler, I. L. Garzon, and L. C. Balbas, Phys. Rev. B 70 (16), 165403 (2004).
[7] M. Neumaier, F. Weigend, O. Hampe, and M. M.Kappes, J. Chem. Phys. 122, 104702 (2005).
[8] Y. Negishi, Y. Nakamura, A. Nakajima and K. Kaya, J. Chem. Phys. 115, 3657 (2001).
[9] P. Weis, O. Welz, E. Vollmer, and M. M. Kappes, J. Chem. Phys. 120, 677 (2004).
[10] D. Ciuparu, R. F. Klie, Y. Zhu, L. Pfefferle, J. Phys. Chem. B 108, 3967-3969 (2004).
[11] B. Kiran, S. Bulusu, H.-J. Zhai, S. Yoo, X. C. Zheng, L.S. Wang, Proc. Natl. Acad. Sci. USA, 102, 961 (2005).
[12] C. Majumder, V. Kumar, H. Mizuseki, Y. Kawazoe, Phys. Rev. B 71, 035401 (2005).
[13] L.-F. Cui, X. Huang, L.-M. Wang, D.Y. Zubarev, A. I. Boldyrev, J. Li, L.-S. Wang, J. Am. Chem. Soc. 128, 8390 (2006).
[14] J. Mühlbach, P. Pfau, K. Sattler, E. Recknagel, Z. Phys. B, 47, 233 (1982).
[15] G. Ganteför, M. Gausa, K.H. Meiwes-Broer, H.O. Lutz, Z. Phys. D. 12, 405 (1989).
[16] Ch. Lüder, K.H. Meiwes-Broer, Chem. Phys. Lett 294, 391 (1998).
[17] Negishi, H. Kawamata, A. Nakajima, K.Kaya, J. Electron Spectroc. Relat. Phenom. 106, 117 (2000).
[18] L.-F. Cui, X. Huang, L.-M. Wang, J. Li, L.-S. Wang, J. Phys. Chem. A. 110, 10169 (2006).

[19] M.A. Sobhy, J.U. Reveles, U. Gupta, S.N. Khanna, A.W. Castleman, Jr., J. Chem. Phys. 130, 054304 (2009).
[20] A.A. Shvartsburg, M.F. Jarrold, Chem. Phys. Lett. 317, 615 (2000).
[21] A. Böttcher, P. Weis, S. Jester, D. Loeffler, A. Bihlmeier, W. Klopper, and M. Kappes, Phys. Chem. Chem. Phys. 7, 2816 (2005).
[22] A.F. Hebard, M.J. Rosseinsky, R. Haddon, D.W. Murphy, S.H. Glarum, T.T.M. Paalstra, A.P. Ramirez, and A.R. Kortan, Nature (London) 350, 600 (1991).
[23] M. Hirscher, M. Becher, J. Nanosci. Nanotechnol. 3, 3 (2003).
[24] A. Touzik, H. Hermann, and K. Wetzig, J. Chem. Phys. 120, 7131 (2004).
[25] B.P. Tarasov, V.N. Fokin, A.P. Moravskii, Yu. M. Shul'ga, Russ. Chem. Bull. 649, 246 (1997).
[26] A.A.Peera, L.B. Alemany, W.E. Billups, Appl. Phys. A 78, 995 (2004).
[27] V.P. Tarasov, Y.B. Muravlev, V.N. Fokin, Y.M. Shulga, Appl. Phys. A, 78, 1001 (2004).
[28] D. Löffler, S. Ulas, P. Weis, A. Böttcher, M.M. Kappes in preparation.
[29] A. Böttcher, P. Weis, S.-S. Jester, M.M. Kappes, J. Chem. Phys. 6, 5213 (2004).
[30] A. J. Stone, D. J. Wales, Chem. Phys. Lett. 128, 501 (1986).
[31] M. Vonderach, O. T. Ehrler, P. Weis and M. M. Kappes, Analytical Chemistry, 2011, in press.